Dyes and Pigments 217 (2023) 111431

Contents lists available at ScienceDirect

Dyes and Pigments

journal homepage: www.elsevier.com/locate/dyepig

Exploring the reactivity of formylporphyrins with 3-(diethylamino)phenol. Synthesis, spectroscopic properties and singlet oxygen generation of a new porphyrin–rosamine conjugate

Carla Queirós [a], Andreia Leite [a,**], Nuno M.M. Moura [b,***], Ana F.R. Cerqueira [b], Vanda V. Serra [c], Maria G.P.M.S. Neves [b], Augusto C. Tomé [b], Ana M.G. Silva [a,*]

[a] LAQV-REQUIMTE, Department of Chemistry and Biochemistry, University of Porto, 4169-007, Porto, Portugal
[b] LAQV-REQUIMTE, Department of Chemistry, University of Aveiro, 3810-193, Aveiro, Portugal
[c] Centro de Química Estrutural, Institute of Molecular Sciences, Instituto Superior Técnico, Universidade de Lisboa, Av. Rovisco Pais 1, 1049-001, Lisboa, Portugal

ARTICLE INFO

Keywords:
Porphyrin derivatives
Rosamines
Photophysical properties
Transition metal complexes
Singlet oxygen generation

ABSTRACT

The design of novel molecular structures with tunable photophysical properties is an important research field for many applications including optoelectronics, sensing and bioimaging. Porphyrin and rhodamine/rosamine derivatives are among the most studied and relevant chemosensors and imaging probes due to their attractive photophysical properties, such as high absorption coefficients and long emission wavelengths. In this work, we present the synthesis and the structural characterization of a new porphyrin–rosamine conjugate **H_2P3** and its related triarylmethane precursors **H_2P1** and **H_2P2**. The photophysical properties of **H_2P1**, **H_2P2** and **H_2P3**, and their ability to chelate iron(III) and copper(II) ions, were evaluated by absorption and emission spectroscopy. The formation of copper(II) complexes was confirmed by electron paramagnetic resonance (EPR), which also allowed the detection of an intense and stable radical signal for the free-base **H_2P3**. Further studies involving the addition of the 2,2,6,6-tetramethylpiperidine spin trap to derivatives **H_2P1**, **H_2P2** and **H_2P3**, showed that only **H_2P3** gives rise to an EPR detectable signal due to a strong generation of singlet oxygen.

1. Introduction

Fluorescent organic dyes are key tools in modern chemical, biochemical and biomedical research. With the development of these challenging scientific fields, new and sophisticated fluorescent dyes with unique and useful attributes are demanded [1–3].

Rhodamines and their rosamine analogues are important classes of organic dyes that possess very attractive photophysical properties including high photostability, long excitation and emission wavelengths and high fluorescence quantum yield. The success of these derivatives as analyte-responsive fluorogenic probes for sensing and imaging is responsible for the interest of the scientific community in exploring structural modifications of the xanthene ring, aiming to obtain new systems with improved fluorescence properties, selectivity, sensitivity, and good reversibility, as well as rapid dynamic responses [4–8]. One of the most relevant modification approaches involves the derivatization of the phenyl ring at position 9 of the xanthene moiety, thereby potentiating the photoinduced electron transfer (PET) mechanism. The PET process occurs from a donor unit (D) to an acceptor unit (A) leading to the formation of a charge-separated state consisting of the donor radical cation and the acceptor radical anion. In rosamine derivatives containing an amino group at the 4-position of the 9-phenyl ring, PET involves an electron transfer from the amino group to the xanthylium moiety, leading to the quenching of the fluorescence of these derivatives [9–11]. Other studies revealed that excited state lifetimes and fluorescence quantum yields are very different in rosamines with phenyl and thienyl substituents, due to a combination of torsional and inductive effects [12].

Porphyrins also present appealing features as fluorescent dyes. These tetrapyrrolic macrocycles, with great structural diversity, present large molar extinction coefficients in the visible region and high fluorescence quantum yields, as well as rich coordination chemistry. Among the

* Corresponding author.
** Corresponding author.
*** Corresponding author.
E-mail addresses: acleite@fc.up.pt (A. Leite), nmoura@ua.pt (N.M.M. Moura), ana.silva@fc.up.pt (A.M.G. Silva).

https://doi.org/10.1016/j.dyepig.2023.111431
Received 22 November 2022; Received in revised form 17 May 2023; Accepted 23 May 2023
Available online 24 May 2023

numerous applications, the porphyrin macrocycle can be used as a functional platform to develop sensors for metal ions and anions, *via* coordination and hydrogen bond interactions, respectively [13], and also as valuable probes for photodiagnosis/fluorescence imaging [14]. In addition, porphyrins have been used as photosensitizers for photodynamic therapy (PDT), mainly due to their ability to generate singlet oxygen *via* photoinduced intersystem crossing [15].

The conjugation of porphyrins with other chemical entities, including rhodamine dyes, has been explored as a strategy to obtain new molecular structures with different electron and energy transfer mechanisms [16]. Indeed, Zhang's group [17] prepared a rhodamine-linked porphyrin dyad, whose fluorescence was effectively quenched and the fluorescence lifetime was significantly reduced by an intramolecular electron transfer process. More recently, Vinogradov and co-workers [18] reported an elegant Pt(II) porphyrin–rhodamine B dyad linked by an oligo-*p*-phenylene bridge, that allows the generation of a phosphorescent triplet state *via* a pathway involving a photoinduced electron transfer process. Also, Neves and co-workers have developed a series of amide-linked porphyrin–rhodamine dyads with peculiar electro-optical properties that include: (i) utmost intense red-shifted electronic transitions beyond the near-infrared region [19], and (ii) sensing ability towards divalent metal ions such as Cu^{2+}, Zn^{2+}, Cd^{2+}, Pb^{2+} and Hg^{2+} [20].

In addition, porphyrin–rhodamine conjugates have also attracted much attention as potent photosensitizers (PS) for PDT, as cationic rhodamines can specifically accumulate in mitochondria, being able to operate as a mitochondrial targeting vector, and since they are able to potentiate the photophysical properties and the singlet oxygen ($^1O_2$) generation [21–25]. In these dyads, the two-photon energy absorbed by the rhodamine moiety is effectively transferred to the porphyrin moiety *via* intramolecular resonance energy transfer [24]. The excited PS then undergoes intersystem crossing to the triplet state, where it can transfer its energy to molecular oxygen, producing reactive oxygen species, such as the highly cytotoxic $^1O_2$, capable of destroying malignant tissues.

Curiously, despite the numerous studies related to porphyrin–rhodamine conjugates, to our knowledge, there are no examples of porphyrin–rosamine structures in the literature. The advantages of using rosamine over rhodamine can be: (i) the rosamine lacks the carboxylate group at the 2-position of the phenyl ring at the 9-position of the xanthene, and therefore it does not participate in spirolactone-quinoid equilibria, which means they are *always-on* and permanently cationic probes and (ii) are easier to synthesize and purify.

Considering our experience with porphyrin and xanthene derivatives, we decided to explore the unprecedented synthesis of new porphyrin–rosamine dyads and explore their optical properties. To do so, we performed the reaction of 3-(diethylamino)phenol with 2-formyl-5,10,15,20-tetraphenylporphyrin. Although **H_2P1** could be obtained in good yield, the corresponding cyclized derivative was not obtained, probably due to steric hindrance effects considering the close proximity of the bulky diarylmethane substituent to the porphyrinic core (Fig. 1). To circumvent this result, condensation of 3-(diethylamino)phenol with 2-(4-formylphenyl)-5,10,15,20-tetraphenylporphyrin was conducted. The resulting **H_2P2** was subsequently subjected to oxidative cyclization using *p*-chloranil to give the desired **H_2P3** conjugate (Fig. 1), which directly links a rosamine moiety to position 2 of the 5,10,15,20-tetraphenylporphyrin.

Compounds **H_2P1**, **H_2P2** and **H_2P3** (Fig. 1) were characterized by NMR and mass spectrometry, and their optical properties (UV–Vis and fluorescence) were studied in several solvents. The interactions of these compounds towards Fe(III) and Cu(II) metal ions were also studied due to their importance in biological and environmental systems. EPR studies were performed to characterize the isolated complexes and also to better understand the interaction of the ligands with the paramagnetic Cu^{2+} ion. Furthermore, during the EPR analysis, the unexpected appearance of a radical signal for the **H_2P3** conjugate was observed. Further studies involving the addition of the 2,2,6,6-tetramethylpiperidine (TEMP) spin trap to derivatives **H_2P1**, **H_2P2** and **H_2P3**, showed that only **H_2P3** leads to the formation of the nitroxyl radical TEMPO, which indicates a strong generation of singlet oxygen by this conjugate.

2. Results and discussion

2.1. Synthesis

The synthetic approach to obtain **H_2P1**–**H_2P3** is outlined in Scheme 1. The starting free-base 2-formyl-5,10,15,20-tetraphenylporphyrin (**TPPCHO**) and its Cu(II) complex **CuTPPCHO** [26] and 2-(4-formylphenyl)-5,10,15,20-tetraphenylporphyrin (**TPP-C_6H_4CHO**) [27] were previous synthesised following reported procedures.

The synthesis of **H_2P1** and **H_2P2** involved the condensation of the appropriate formyl-porphyrin derivative with 5 equivalents of 3-(diethylamino)phenol in the presence of a catalytic amount of 4-methylbenzenesulfonic acid (10 mol%) in a mixture of toluene/propanoic acid (2:1) at reflux. The reaction with **CuTPPCHO** afforded, after 4 h, a main product that, based on its mass spectrum ($m/z = 1016.5$), was identified as the expected **CuP1** (Scheme 1A). This compound was isolated in 85% yield. All attempts to convert **CuP1** into the corresponding **CuPorph-**

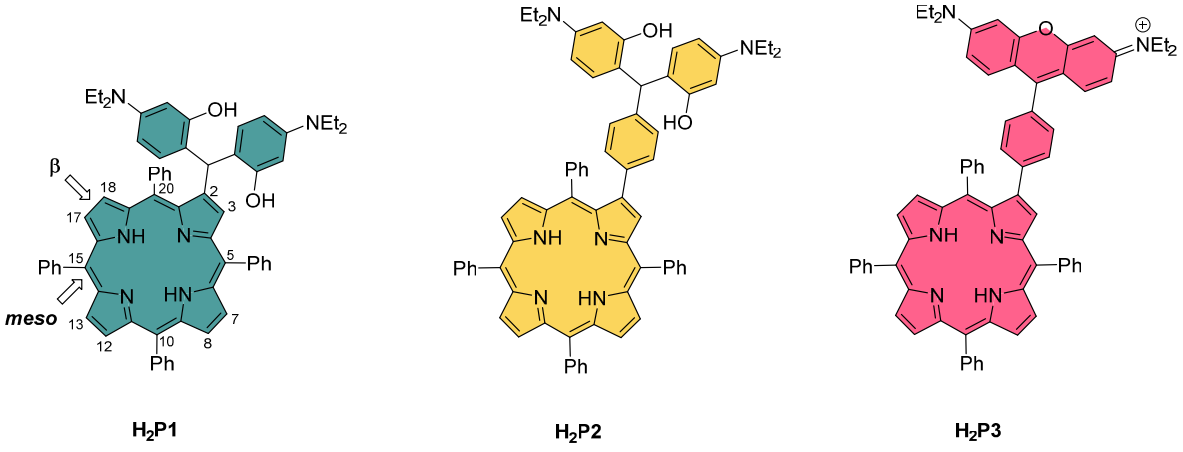

Fig. 1. Porphyrin derivatives **H_2P1**, **H_2P2** and **H_2P3**.

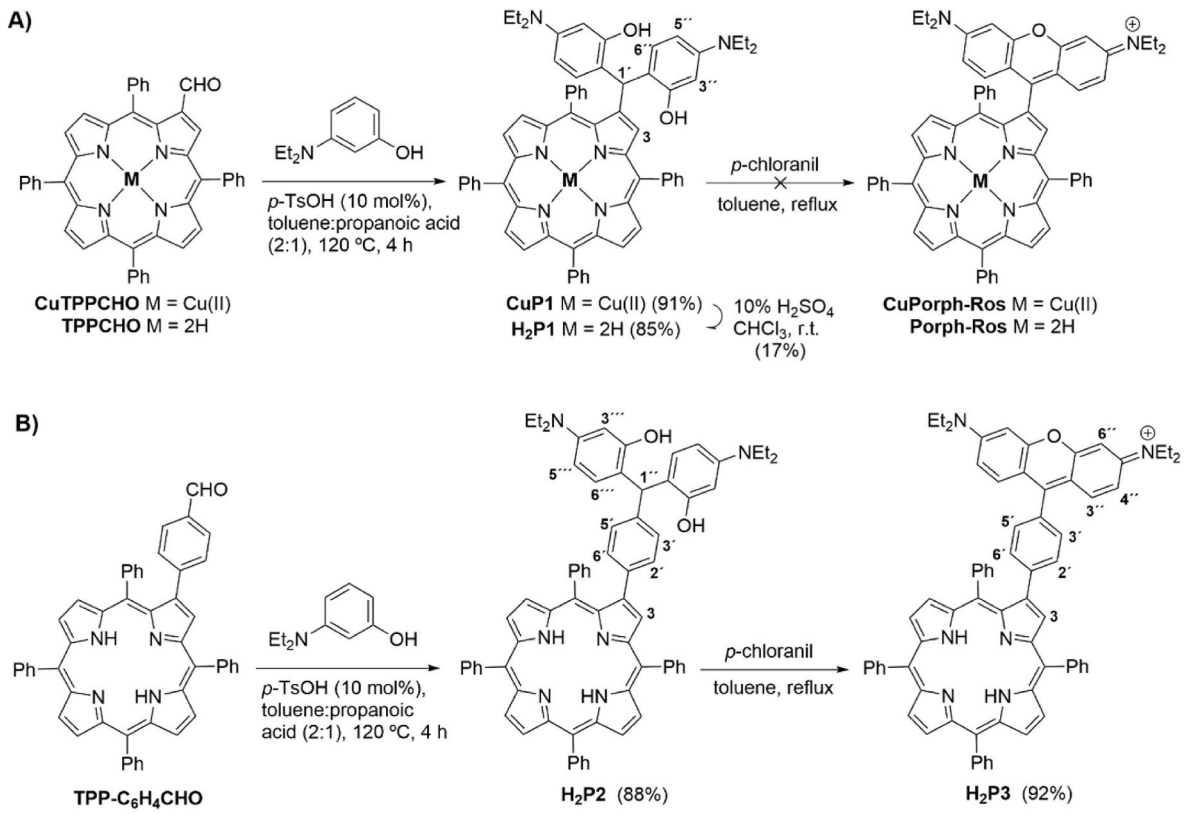

Scheme 1. Synthetic approaches to prepare **H_2P1**, **H_2P2** and **H_2P3**.

Ros under oxidative conditions (e.g., *p*-chloranil in refluxing toluene) were unsuccessful and the starting material was recovered.

This fact prompted us to try the oxidative step using the corresponding free-base **TPPCHO** considering that the presence of the metal in the porphyrin inner core was, in some way, limiting the external group to acquire the adequate conformation for the required oxidative cyclization step. Since the demetallation reaction of the **CuP1** derivative under conventional acidic conditions (10% H_2SO_4 in $CHCl_3$) [28] provided the required **H_2P1** in unacceptable yield (17%) for further studies, we decided to perform the condensation reaction of 3-(diethylamino) phenol with the free-base **TPPCHO** (Scheme 1A). After 4 h at 120 °C, the free-base **H_2P1** was isolated with an excellent 91% yield. This compound was then treated with *p*-chloranil in refluxing toluene but the desired oxidative cyclization did not occur and, again, only the starting porphyrin derivative **H_2P1** could be isolated. Other conditions, including the use of 2,3-dichloro-5,6-dicyano-1,4-benzoquinone (DDQ) as oxidant in refluxing toluene or by heating **H_2P1** in 1,2,4-trichlorobenzene at reflux, conducted to complex mixtures of compounds enabling further purification.

Considering that the difficulties experienced in the synthesis of a porphyrin derivative with a xanthene moiety directly linked to the porphyrin macrocycle are probably due to steric hindrance effects, we decided to try the previous conditions but using the 2-(4-formylphenyl)-5,10,15,20-tetraphenylporphyrin (Scheme 1B). It was expected that a 1,4-phenylene group between the porphyrin macrocycle and the xanthene ring could allow the formation of **H_2P3**.

In order to avoid potential drawbacks during the removal of Cu(II), these studies were performed using the free-base **TPP-C_6H_4CHO**. The condensation with 3-(diethylamino)phenol afforded, after 4 h at 120 °C, the desired derivative **H_2P2** as the solo product and in excellent yield (88%). Porphyrin **H_2P2** was then successfully oxidized to the desired porphyrin–rosamine conjugate **H_2P3** with *p*-chloranil in refluxing toluene for 1 h. The excellent yield obtained for **H_2P3** (92%) confirmed that the unsuccessful formation of the porphyrin–rosamine dyad from **H_2P1** is probably related to steric strain; the close proximity of the bulky porphyrin macrocycle prevented the successful oxidative cyclization or conducted to non-desired reactions.

The structures of **H_2P1**, **H_2P2** and **H_2P3** were confirmed by NMR spectroscopy (^{1}H and ^{13}C) and mass spectrometry (see Figs. S2–S15, Supporting information). The ^{1}H NMR spectra of **H_2P1** and **H_2P2** exhibit a singlet at around δ 5.5 ppm due to the resonance of the benzylic proton. In the ^{1}H NMR spectrum of **H_2P1** a broad singlet at δ 4.77 ppm, due to the resonances of the protons from the hydroxy groups, and a quartet at around δ 3.3 ppm and a triplet at *ca.* δ 1.2 ppm, due to the resonances of the protons from the diethylamino moieties, are observed. The signals due to the resonances of the *beta*-pyrrolic protons are the most deshielded ones and appear between δ 8.97 ppm and δ 8.46 ppm. The protons from the *meso*-phenyl groups appear as multiplets between *ca.* δ 8.4 ppm and δ 7.3 ppm. For the **H_2P1** derivative, the resonances of the aromatic protons from the (diethylamino)phenol units generate two doublets at δ 6.32 ppm and δ 5.88 ppm, with a coupling constant of J 8.4 Hz, and a singlet at δ 6.20 ppm. For the **H_2P2** derivative, and comparing with the spectrum of **H_2P1**, the protons from the equivalent units are more deshielded, appearing in the range from δ 7.40 ppm to δ 6.78 ppm. The ^{1}H NMR spectrum of the **H_2P2** displays an additional multiplet ranging from δ 6.5 ppm to δ 6.1 ppm due to the resonances of the protons from the 1,4-phenylene group. For compound **H_2P2** the signals attributed to the resonances of the diethylamino moieties appear as multiplets at δ 3.55–3.25 ppm and δ 1.28–1.06 ppm assigned to the formation of atropoisomers due to the hindered rotation related with the steric repulsion between the substituents at the diethylamino moieties.

Comparing the spectra of the porphyrin–rosamine conjugate **H_2P3** and the corresponding precursor **H_2P2**, the most remarkable difference is the absence of the benzylic proton. The ^{1}H NMR spectra of all free base derivatives display the characteristic peak at *ca.* δ - 2.6 ppm due to the resonances of the *N*–H protons at the porphyrin inner core.

The mass spectra of the non-cyclized derivatives display a peak corresponding to the $[M + H]^+$ ion, while the mass spectrum of the

porphyrin–rosamine conjugate exhibits the peak corresponding to the $[M]^+$ ion.

2.2. Optical properties of the porphyrin derivatives H_2P1– H_2P3

The spectrophotometric measurements for compounds **H_2P1**– **H_2P3** were undertaken in anhydrous dichloromethane, anhydrous methanol, water and 3-(*N*-morpholino)propanesulfonic acid (MOPS), pH = 7.40, 0.1 M NaCl at 25 °C. For comparison purposes, the same was performed for **RosH** and 5,10,15,20-tetraphenylporphyrin (**TPP**) (Fig. S1). The photophysical data obtained in dichloromethane were more interesting, namely in terms of fluorescence quantum yield, and are reported in Table 1. The results for the other solvents are included in the Supporting information (Table S1).

Fig. 2 shows the absorption and emission spectra of **H_2P1**, **H_2P2** and **H_2P3** in dichloromethane. **H_2P1** and **H_2P2** absorption spectra show the characteristic bands of free base *meso*-tetraarylporphyrin derivatives with the intense Soret band at 419 and 421 nm, respectively, associated to the allowed transition from $S_0 \rightarrow S_2$; the four Q-bands of weak intensity and associated to $S_0 \rightarrow S_1$ transitions, appear between 518 and 646/649 nm. **H_2P3** also shows the Soret band at 421 nm, however, the region between 519 and 557 nm presents some differences associated with the presence of the xanthene ring, as can be deduced by comparison with the **RosH** absorption bands. The band at 557 nm overlaps with the 2nd and 3rd Q-bands, nevertheless, the first and 4th bands are visible in the same region of **H_2P2** (518 and 649 nm). Compared with **TPP**, the Soret bands of compounds **H_2P1**, **H_2P2** and **H_2P3** show a slight red shift of 2–4 nm, which can be caused by the steric hindrance and electron effects of the β-substituents in the porphyrin ring [30].

The emission spectra of **H_2P1** and **H_2P2** show two bands characteristic of porphyrin derivatives, one at 652/657 nm and the other, of lower intensity, at 716/720 nm, which are similar to the **TPP** emission bands. In contrast, the porphyrin–rosamine conjugate **H_2P3** exhibits poor emission efficiency in solution, as evidenced by its low fluorescence quantum yield and the absence of measurable emission bands. Several values of fluorescence quantum yield are presented in the literature for **TPP** [29], but the value 0.11 is the most frequently used as reference. Taking this value into consideration, it is clear that the presence of the xanthene ring in **H_2P3** affects severely its quantum yield. Similar fluorescence quenching behaviours have also been reported for rhodamine–porphyrin dyads and attributed to electron and energy transfer processes between the porphyrin and rhodamine units [17]. Fluorescence lifetime decays obtained for **H_2P3** also confirm the presence of the rosamine and porphyrin units in this conjugate (See SI Table S2 and Fig. S20 for more details).

Table 1
Optical properties of **H_2P1–H_2P3**, and also of **TPP** and **RosH**, in CH_2Cl_2.

Compound	λ_{abs}/nm	ε ($\times 10^3$)/ $mol^{-1}dm^3cm^{-1}$	λ_{em}/ nm	Stokes Shift/ cm^{-1}	Φ_F
H_2P1	419, 443, 518, 550, 593, 646	379, 17.2, 21.1, 6.35, 6.58, 1.45	652 716	142	0.03
H_2P2	421, 518, 554, 594, 649	349, 17.1, 4.95, 6.92, 4.74, 2.75	657 720	188	0.06
H_2P3	421, 519, 557, 649	279, 40.1, 98.8, 5.05	658 718	211	0.02
TPP	417 (shoulder 401), 514, 549, 599, 647	449, 18.7, 7.85, 3.92, 6.65	651 715	95	0.04–0.15 [29]
RosH	557 (shoulder 520)	751	574	532	0.56 [9]

2.3. Spectrophotometric and spectrofluorimetric titrations and metal-interaction effects

The complexation of transition metal ions at the porphyrins core has been used as a recurrent strategy to adjust the electronic and photophysical properties of these compounds. In this work, we decided to focus on the complexation of the newly synthesised porphyrins with the bivalent transition metal ion Cu^{2+} (d^9 configuration) and the trivalent Fe^{3+} (d^5 configuration). These metal ions were selected primarily because they play important roles in biological and environmental systems, and also because they represent two important classes of metal ions with different oxidation states, which can lead to the formation of different complexes through coordination with porphyrins, either in their periphery or in the inner core.

The interaction of **H_2P1**, **H_2P2** and **H_2P3** with Fe^{3+} and Cu^{2+} – up to 10 equiv. – was investigated by the titration of each porphyrin derivative, dissolved in anhydrous dichloromethane, with the adequate metal salt dissolved in anhydrous methanol. The titrations were monitored by UV–Vis and fluorescence emission spectroscopy, at 298 K. Considering that some counterions, such as chloride, might affect the metal ion interaction with porphyrins [31], trifluoromethanesulfonate salts were chosen to perform these studies.

2.3.1. Titration with Fe^{3+}

The titration of porphyrins with Fe^{3+} led to significant changes in the absorption and emission profiles. The absorption spectra of **H_2P1** and **H_2P3** with increasing amounts of Fe^{3+} are presented in Fig. 3. The spectrum for **H_2P2**, being very similar to **H_2P1**, is presented in the SI (Fig. S17). From the analysis of the spectra, it is evident that Fe^{3+} interacts similarly with the three porphyrin derivatives: i) a red shift of the Soret band occurs from 419 to 444 nm (**H_2P1**), 421–445 nm (**H_2P2**), and from 421 to 441 nm (**H_2P3**); ii) the number of Q bands decreases, from four to one, due to the increase in symmetry of the metallated porphyrin, being perceptible a band at 661 nm for **H_2P1** and at 666 nm for **H_2P2** and **H_2P3**. This red shift of the Soret band, accompanied by the formation of a new absorption band at a longer wavelength, can be justified considering the formation of sitting-atop (SAT) complexes, where the coordination of the metal ion to the porphyrin nitrogen atoms occurred without their deprotonation [32–37].

For **H_2P3**, the absence of changes in the band at 557 nm, associated to the xanthene moiety, is a clear statement of the lack of interaction of the xanthene ring with the metal ion. The presence of well-defined isosbestic points around 430, 431 and 434 nm for **H_2P1**, **H_2P2** and **H_2P3**, respectively, allows better visualization of the decrease of the Soret band of the metal-free forms and the appearance of a prominent band at *ca.* 445 nm.

In terms of fluorescence emission, the spectra reveal for **H_2P1**: i) fluorescence intensity quenching of the two emission bands at 651 and 716 nm, when λ_{exc} = 419 nm, up to 7 equiv. of Fe^{3+} and the merge of the two bands in one, around 694 nm, for higher Fe^{3+} equiv. and ii) fluorescence intensity enhancement (200 times) of a new emission band at 701 nm when λ_{exc} = 661 nm (Fig. 4, for **H_2P1**). Similar behaviour is observed for **H_2P2**, the corresponding spectra are presented in the SI (Fig. S18). For **H_2P3**, no measurable fluorescence emission was obtained before and after the addition of Fe^{3+}. At this point, through the interaction of the porphyrin core with Fe^{3+}, we expected to perturb the electron and energy transfer processes between the porphyrin and the rosamine units. However, as evidenced by the weak fluorescence observed, this was not the case. Considering this, and looking at the structural features of **H_2P3**, we suggest that there is a strong twist between the porphyrin and the rosamine units, consistent with a twisted intramolecular charge transfer (TICT) mechanism [38,39], which may be responsible for the permanence of the fluorescence quenching state of **H_2P3**.

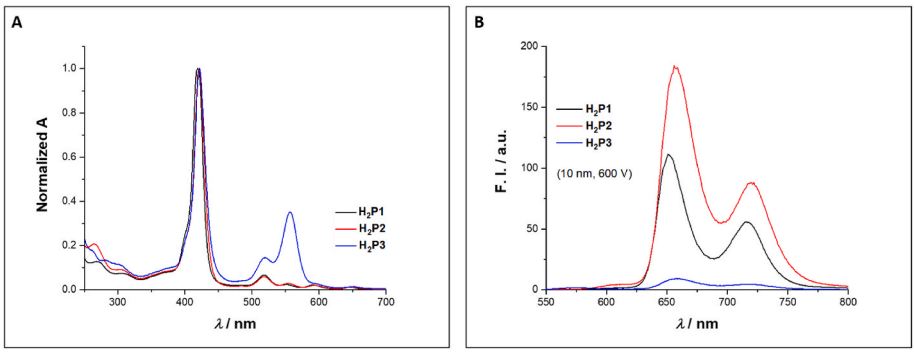

Fig. 2. Absorption (**A**) and emission (**B**) spectra of **H_2P1** (black), **H_2P2** (red) and **H_2P3** (blue) in anhydrous dichloromethane (**H_2P1** $\lambda_{exc} = 419$ nm, **H_2P2** and **H_2P3** $\lambda_{exc} = 421$ nm); [**H_2P1**] = 2.93 μmol dm^{-3}, [**H_2P2**] = 2.84 μmol dm^{-3} and [**H_2P3**] = 3.11 μmol dm^{-3} for absorption spectra and [**H_2P1**] = 0.29 μmol dm^{-3}, [**H_2P2**] = 0.28 μmol dm^{-3} and [**H_2P3**] = 0.31 μmol dm^{-3} for emission spectra.

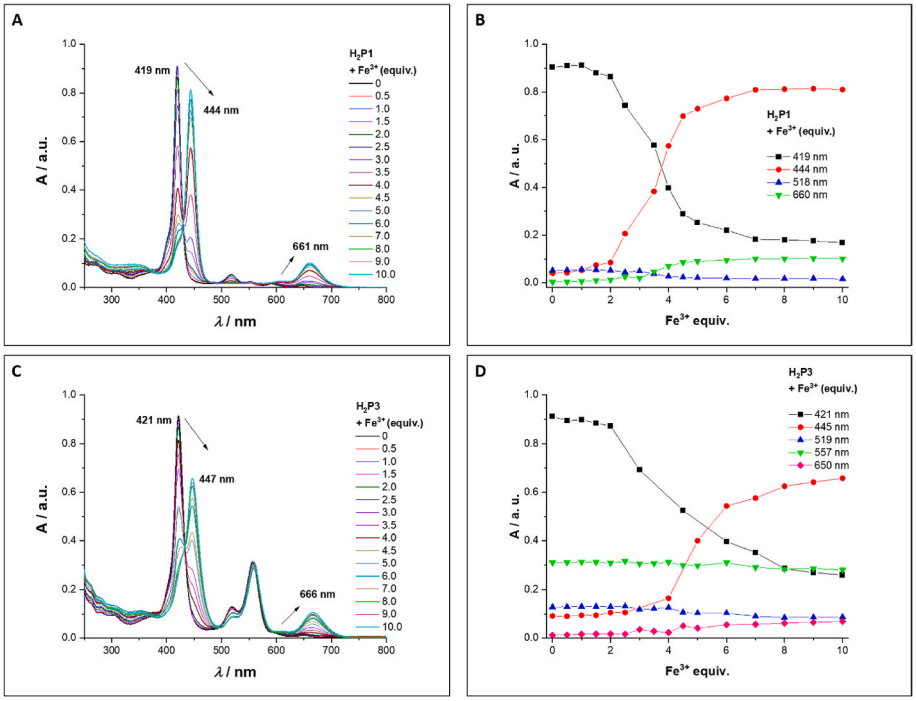

Fig. 3. Spectrophotometric titrations of **H_2P1** (A and B) and **H_2P3** (C and D) in dichloromethane as a function of added iron(III) trifluoromethanesulfonate in methanol, at 298 K [**H_2P1**] = 2.81 μmol dm^{-3}, [**H_2P3**] = 2.99 μmol dm^{-3}.

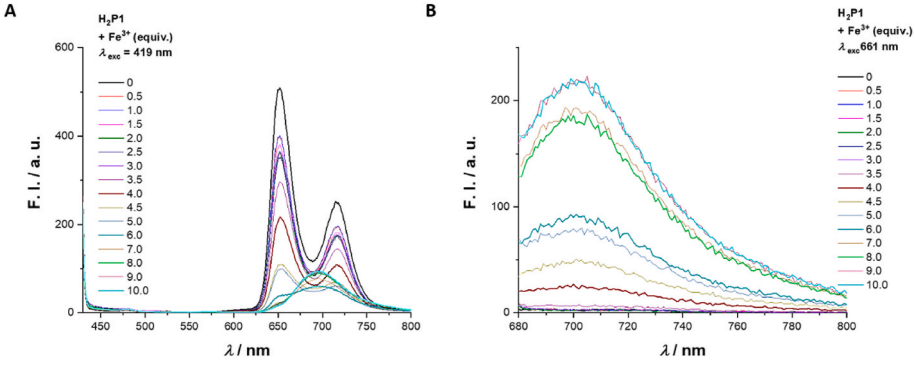

Fig. 4. Spectrofluorimetric titration of **H_2P1** in dichloromethane as a function of added iron(III) trifluoromethanesulfonate in methanol, at 298 K [**H_2P1**] = 0.28 μmol dm^{-3}; $\lambda_{exc} = 419$ nm (A) and [**H_2P1**] = 2.81 μmol dm^{-3}; $\lambda_{exc} = 661$ nm (B).

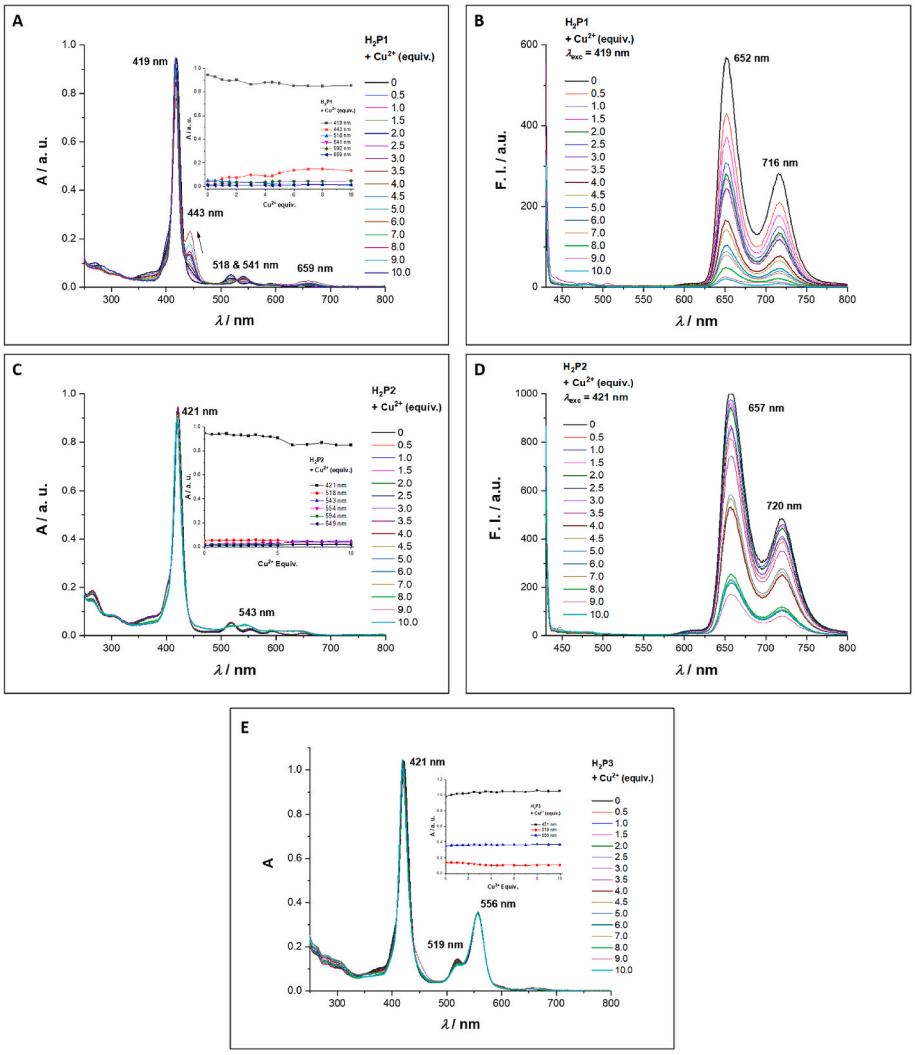

Fig. 5. Spectrophotometric (A, C and E) and spectrofluorimetric (B and D) titrations of **H_2P1** (A and B), **H_2P2** (C and D) and **H_2P3** (E) in dichloromethane as a function of added copper(II) trifluoromethanesulfonate in methanol, at 298 K. The insets show the absorption at 419, 443, 518, 541, 592 and 659 nm (**H_2P1**); 421, 518, 543, 554, 594 and 649 nm (**H_2P2**) and 421, 519 and 556 nm (**H_2P3**). [**H_2P1**] = 2.81 μmol dm^{-3}; [**H_2P2**] = 2.76 μmol dm^{-3} and [**H_2P3**] = 3.11 μmol dm^{-3} (absorption spectra, A, B and E) and [**H_2P1**] = 0.28 μmol dm^{-3}; λ_{exc} = 419 nm (B), [**H_2P2**] = 0.28 μmol dm^{-3}; λ_{exc} = 421 nm (D) (emission spectra).

2.3.2. *Titration with Cu^{2+}*

A similar spectroscopic study was performed for Cu^{2+} with **H_2P1**–**H_2P3**. In contrast to Fe^{3+}, the addition of Cu^{2+} leads to smaller variations in the intensity of the absorption bands for all derivatives (Fig. 5 and Fig. S19 in Supporting information). The titration of **H_2P1** with Cu^{2+} induces a two-step change in the absorption spectrum. In the first part, the appearance of two new bands at 443 and 659 nm suggests the formation of a SAT complex, which is followed in the second part by the insertion of the Cu^{2+} in the porphyrin inner core with the expected elimination of the two protons. This is corroborated by the profile of the final spectrum showing the Soret band with a 2 nm hypsochromic shift and the appearance of a new band at 543 nm typical of a metalloporphyrin. For **H_2P2**, the Soret band remains practically with the same intensity and the Q bands collapse from 4 bands to one new band at 543 nm, while the band at 520 nm is still observed, which seems to indicate that the insertion of Cu^{2+} is not total.

For **H_2P3**, only small differences are observed in the absorption spectra, and considering the presence of the two bands at 519 and 557 nm associated to the rosamine contribution, it was not possible to extract more information about the porphyrin Q bands. In terms of fluorescence emission, again no relevant emission was observed for **H_2P3** (no spectra are presented) and a fluorescence intensity quenching occurs for **H_2P1** (Fig. 5B, bands at 652 and 716 nm) and **H_2P2** (Fig. 5D, bands at 657 and 720 nm) with increasing amounts of Cu^{2+}, although no new bands are observed even after the addition of 10 equivalents.

Considering the behaviour differences between the Fe^{3+} and Cu^{2+} complexes, we decided to confirm if the interactions of ligands in solution with Cu^{2+} are consistent with their behaviour in the isolated complexes. To do that, the UV–Vis, fluorescence and EPR features of the Cu^{2+} complexes of **H_2P1**, **H_2P2** and **H_2P3** isolated (powder) were analysed.

2.4. *Optical properties of the Cu^{2+} complexes*

The Cu^{2+} complexes of **H_2P1**, **H_2P2** and **H_2P3** were prepared as described in the experimental section and their photophysical properties were evaluated in dichloromethane (Table 2 and Fig. 6).

Comparing the absorption spectra of the Cu^{2+} complexes formed during titrations (10 equiv.) and those of the Cu^{2+} complexes isolated, we can observe the same bands, with small shifts, 417 and 541 nm for **CuP1** (419 and 541 in solution), 419 and 542 nm for **CuP2** (421 and 543 nm in solution) and 418 and 556 nm for **CuP3** (421 and 556 nm in solution). This proves the formation of the copper complexes during

Table 2
Photophysical properties of complexes **CuP1**, **CuP2** and **CuP3** in dichloromethane (298 K).

Complex	λ_{abs}/nm	ε/mol^{-1}dm^{3}cm^{-1}
CuP1	417, 541	3.16×10^5, 1.82×10^4
CuP2	419, 542	2.02×10^5, 1.09×10^4
CuP3	418, 556 (shoulder 516)	2.01×10^5, 6.93×10^4

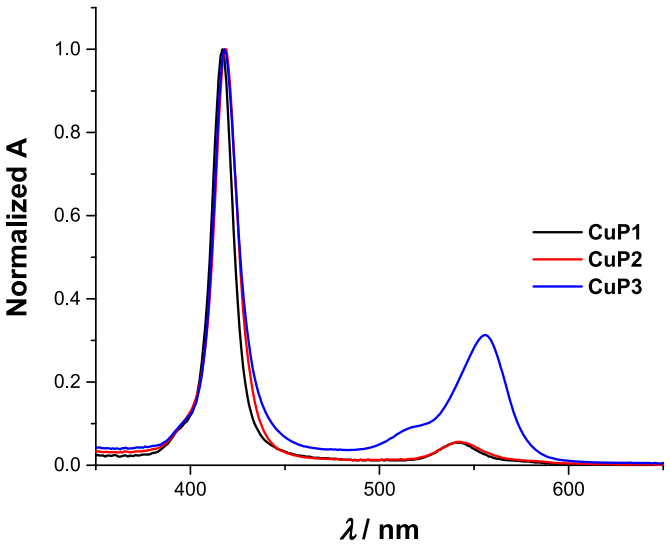

Fig. 6. Absorption spectra of **CuP1** (black line), **CuP2** (red line) and **CuP3** (blue line) in anhydrous dichloromethane at 298 K ([**CuP1**] = [**CuP2**] = 1.4 μmol dm^{-3}, and [**CuP3**] = 1.5 μmol dm^{-3}).

titrations. The emission for all Cu^{2+} complexes is negligible, as expected for a paramagnetic metal ion.

2.5. EPR studies

To access information about the coordination sites of **H_2P1**, **H_2P2** and **H_2P3**, EPR studies were performed on the Cu^{2+} complexes (**CuP1**, **CuP2** and **CuP3**). The EPR spectra of these complexes, obtained in DMSO/CH_2Cl_2 (1:1) at 100 K, are depicted in Fig. 7.

Spectra signals are similar in the three conjugates and characteristic of one electron ($S = 1/2$) Cu^{2+} system and exhibit lines attributed to the hyperfine interaction of the unpaired electron with the copper nucleus ($I = 3/2$) and superhyperfine interaction with the four nitrogen atoms ($I = 1$) of the porphyrin macrocycle. For all conjugates, no Cu^{2+} coordination to the free oxygens was observed. To evaluate if *O* coordination could be detected for higher amounts of Cu^{2+}, titration of **H_2P1** and **H_2P2** with increasing amounts of Cu^{2+} was performed from 1:0 to a 1:10 M ratio [40]. For compounds **H_2P1** and **H_2P2**, the study revealed that no *O* coordination occurred. Computer simulation considering the above interactions allowed a good fitting with the experimental spectra for all compounds. In Fig. S21 and Table S3 (SI) are presented the spin-Hamiltonian parameters and computational simulation for **CuP3**. The components of the *g* and *A* tensors for all complexes are consistent with an axial ($g_x = g_y$) complex and very similar to those obtained in a previous work regarding a set of porphyrins functionalized with 3-hydroxy-4-pyridinone ligands [41].

During the titration experiments regarding the interaction between **H_2P1**, **H_2P2** and **H_2P3** with Cu^{2+} and considering the initial measurements in the absence of copper, a very weak signal was obtained for compounds **H_2P1** and **H_2P2**, but a strong signal, typically attributed to radical species, was observed for **H_2P3** (Fig. 8).

Porphyrins with different *meso*-substituted groups can originate EPR signals since these molecules display a cyclic highly conjugated system. For non-metallated, porphyrins the EPR signals observed can be attributed to two effects: (a) interaction of unpaired π electrons with the nuclear spin of the nitrogen atoms in the porphyrin ring and/or (b) due to the presence of reversibly absorbed oxygen in the porphyrin ring. Since **H_2P3** presents a very narrow EPR signal with a g value typical of organic radicals this signal can be attributed to the interaction between **H_2P3** and oxygen, that is reversibly absorbed in the porphyrin ring [30,42].

Then, taking into consideration that porphyrin derivatives can generate reactive oxygen species (ROS), namely singlet oxygen ($^1O_2$),

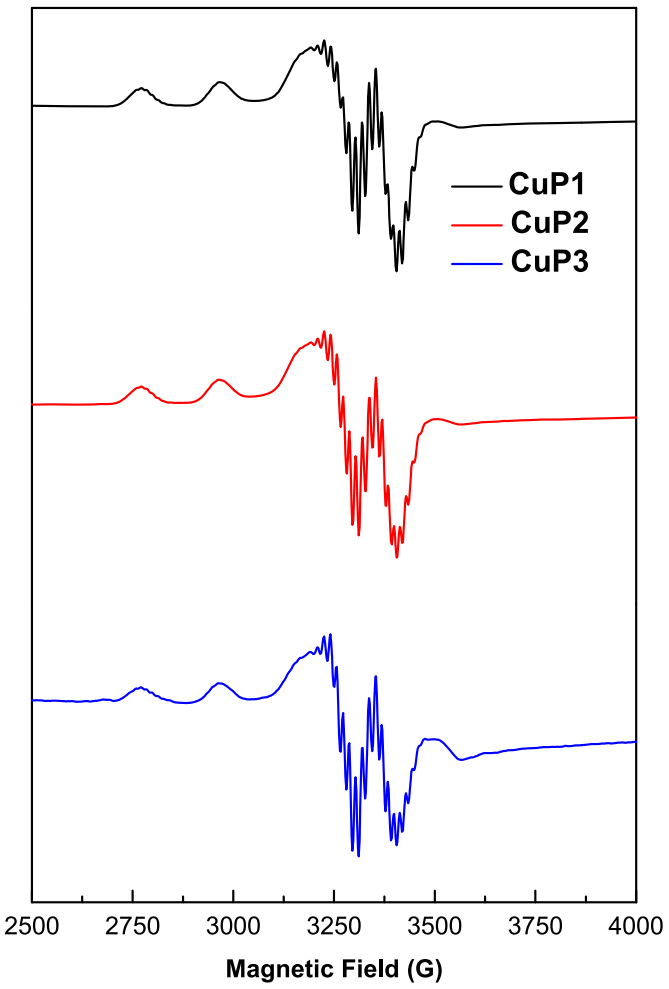

Fig. 7. X-band EPR spectra of **CuP1** (black line), **CuP2** (red line) and **CuP3** (blue line) obtained in a DMSO/CH_2Cl_2 (1:1) frozen matrix.

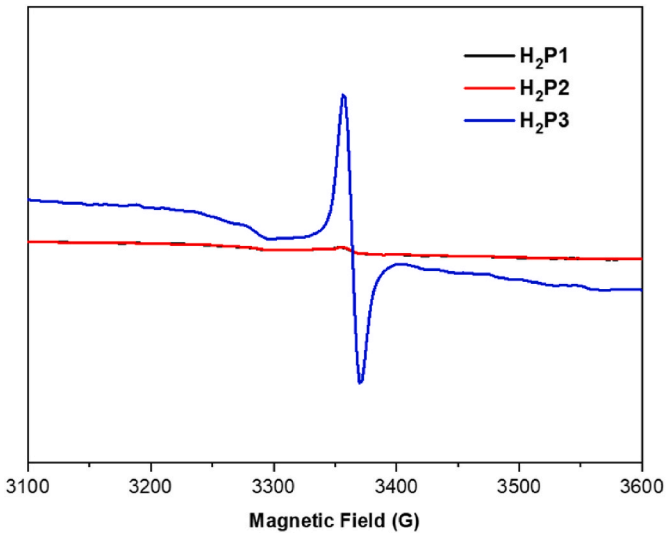

Fig. 8. X-band EPR spectra of **H_2P1** (black line), **H_2P2** (red line) and **H_2P3** (blue line) obtained in a DMSO/CH_2Cl_2 (1:1) frozen matrix.

EPR trapping studies for **H_2P3** were performed using the spin trap 2,2,6,6-tetramethylpiperidine (TEMP) as a specific probe for the detection of $^1O_2$. The spectra of the spin trap and compounds **H_2P1** and **H_2P2**

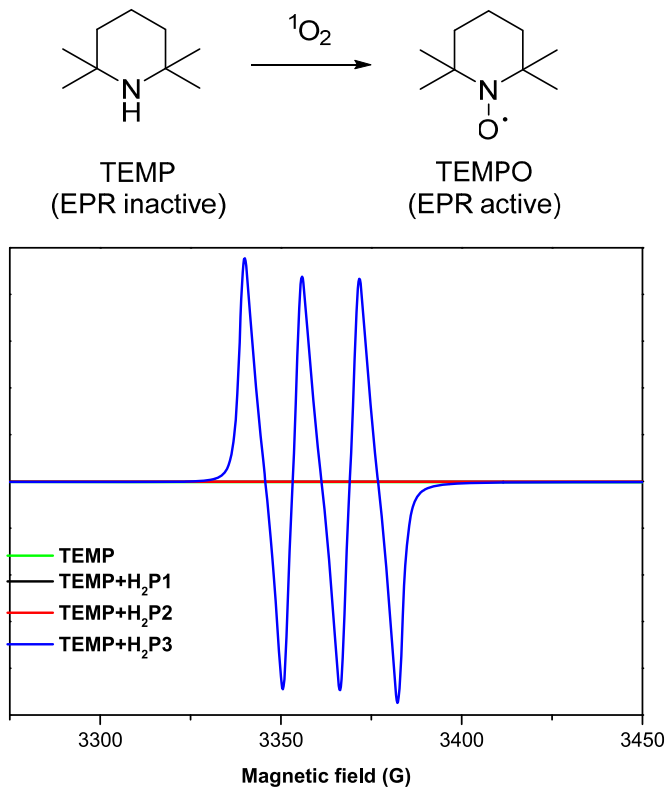

Fig. 9. Spectra of TEMP (green line), **H_2P1** (black line), **H_2P2** (red line) and **H_2P3** (blue line) at room temperature.

were also acquired as a control. When $^1O_2$ is produced, it can react with TEMP to form the stable nitroxyl radical TEMPO. In Fig. 9, it can be observed that only for compound **H_2P3** the signal attributed to the radical TEMPO can be observed, which indicates the presence of $^1O_2$. For compounds **H_2P1** and **H_2P2** no signal is observed indicating that, under the used conditions, no $^1O_2$ is produced.

The production of $^1O_2$ is regulated by the photophysical parameters of the photosensitizer, where the presence of substituents can exert a strongly positive effect on the required non-radiative transition intersystem crossing from its singlet excited state into the triplet state. Then, the photosensitizer in its excited triplet state reacts directly with molecular oxygen in the triplet ground state, $^3O_2$, resulting in the generation of singlet excited state of molecular oxygen ($^1O_2$). In this work, the presence of the rosamine moiety in **H_2P3** favors, under EPR conditions [30,43], the formation of a porphyrin radical which is responsible by an efficient singlet oxygen generation *via* the triplet-triplet annihilation process [44]. On the other hand, the efficiency of $^1O_2$ generation is strongly dependent on the porphyrin chemical structures [42], often promoted by the presence of larger substituent groups at the peripheral positions of the macrocycle [30]. In our case, it is very evident that the introduction of the rosamine unit in the *β*-position of the porphyrin results in electron and stereo effects that strongly promote the generation of $^1O_2$. Considering these results, further studies are currently being performed to better understand the generation of the reactive oxygen species under EPR conditions, including the comparison with other porphyrin derivatives.

3. Conclusions

A new porphyrin–rosamine conjugate **H_2P3** was synthesised through the condensation of 3-(diethylamino)phenol with 2-(4-formylphenyl)-5,10,15,20-tetraphenylporphyrin, followed by the oxidative cyclization of the intermediate **H_2P2**. The studies showed that the required oxidative cyclization is limited by the proximity of the bulky bis(4-(diethylamino)-2-hydroxyphenyl)methyl unit to the porphyrin core, preventing the formation of the desired conjugate porphyrin–rosamine from **H_2P1**.

The optical properties of the new porphyrin derivatives **H_2P1**–**H_2P3** and their ability to chelate Fe(III) and Cu(II) were assessed by absorption and fluorescence emission, in dichloromethane, considering the most favourable fluorescence quantum yield values obtained in this solvent. Significant changes in the absorption and fluorescence spectra of **H_2P1**, **H_2P2** and **H_2P3** were observed with increasing amounts of Fe^{3+}, suggesting that the interaction occurs without deprotonation of the porphyrin inner core, resulting in the formation of SAT complexes, while for Cu^{2+}, the formation of the metalloporphyrins is observed, particularly when a large excess of Cu^{2+} is used. Such differences in the metal ion interactions of the derivatives can be related with the difference in the oxidation state of the two metals.

The Cu^{2+} complexes of all derivatives (**H_2P1– H_2P3**) were characterized by EPR confirming the coordination of Cu^{2+} to the four nitrogen atoms of the porphyrin core, while no coordination of Cu^{2+} to the oxygen atoms of the phenol substituents in derivatives **H_2P1** and **H_2P2** was observed.

According to the EPR measurements performed in the absence of any spin-trapping agent, a strong EPR signal corresponding to a free radical was observed for the free-base conjugate **H_2P3**, while a weak signal was detected for **H_2P1** and **H_2P2**. However, after titrating **H_2P1**, **H_2P2** and **H_2P3** with copper(II) ion, the EPR signals obtained are all similar because the intensity of the EPR signal generated by the copper(II) ion is so high that it covers the EPR signal of **H_2P3**. On the other hand, EPR trapping studies with conjugate **H_2P3** using the spin-trapping agent TEMP, showed an intense signal attributed to the radical TEMPO, which revealed the formation of singlet oxygen.

The results obtained revealed that the electronic and stereo effects due to the rosamine unit linked to the *β*-pyrrolic position of the porphyrin strongly influence the EPR, UV–Vis and fluorescence emission spectra of **H_2P3**. Thus, **H_2P3** can be considered an attractive probe or photosensitizer for biological applications.

4. Experimental section

4.1. Materials and methods

Iron(III) and copper(II) trifluoromethanesulfonate, anhydrous dichloromethane, anhydrous methanol (MeOH), 3-(*N*-morpholino)propanesulfonic acid hemisodium salt (MOPS) and sodium chloride were obtained from Merck and used as received.

^1H and ^{13}C NMR spectra were recorded on Bruker Avance 300 (300.13 and 75.47 MHz, respectively) spectrometer. $CDCl_3$ was used as solvent and tetramethylsilane (TMS) as internal reference; the chemical shifts are expressed in *δ* (ppm) and the coupling constants (*J*) in Hertz (Hz).

Electrospray ionization mass spectra were acquired with a Micromass Q-Tof 2 (Micromass, Manchester, UK), operating in the positive ion mode, equipped with a Z-spray source, an electrospray probe and a syringe pump. Source and desolvation temperatures were 80 °C and 150 °C, respectively. Capillary voltage was 3000 V. The spectra were acquired at a nominal resolution of 9000 and at cone voltages of 30 V. Nebulization and collision gases were N_2 and Ar, respectively. Porphyrin solutions in methanol were introduced at a 10 μL/min flow rate. Mass spectra HRMS-ESI(+) were recorded on a LTQ Orbitrap XL mass spectrometer (Thermo Fischer Scientific, Bremen, Germany) using methanol as solvent.

Electronic absorption spectra were recorded with a Varian Cary bio50 spectrophotometer (Agilent Technologies, Santa Clara, CA, USA), equipped with a Varian Cary single-cell Peltier accessory, using 1 cm path-length quartz cells. Steady-state fluorescence measurements were carried out in a Varian spectrofluorometer, model Cary Eclipse (Agilent Technologies, Santa Clara, CA, USA), equipped with a constant-

temperature cell holder (Peltier single-cell holder) with 5 nm slit width for excitation and emission. All photophysical assays were performed under controlled temperature conditions (25 °C), using the maximum λ_{exc} and the appropriate λ_{em} range, for each compound and considering the different solvents used. Compounds stock solutions were prepared in anhydrous dimethyl sulfoxide (DMSO). Fluorescence quantum yields were determined using a Quantaurus-QY C11347-11 spectrometer (absolute luminescence quantum yield spectrometer).

Fluorescence lifetimes were obtained with a time-correlated single-photon counting (TC-SPC) technique using a commercial equipment FluoroLog-3 spectrofluorimeter (Horiba Jobin Yvon). Excitation at 445 and 594 nm was achieved using a NanoLED (fwhm<1.0 ns) at a repetition rate of 1 MHz. Typical measurements involved accumulation of a maximum count per channel of 10 000. The instrument response function was obtained with a suspension of Ludox (colloidal silica beads) in water. Data analysis was performed with the software package Fluofit version 4.2 from PicoQuant. The goodness of the fit was evaluated by the usual statistical criteria and by visual inspection of the weighted residuals distribution.

Electron paramagnetic resonance (EPR) spectra were recorded using an X-band (9 GHz) Bruker ELEXSYS E 500 spectrometer equipped with a variable temperature unit (ER4B1 VT), obtained under the following general experimental conditions: i) for Cu^{2+} complexes: a microwave frequency of 100 kHz, a microwave power of 20 mW, a modulation amplitude of 8 G, a gain of 60 dB, and an acquisition time of 300 s, at 100 ± 1 K; ii) for spin-trapping assays: a microwave frequency of 100 kHz, a microwave power of 20 mW, a modulation amplitude of 2 G, a gain of 60 dB, and an acquisition time of 300 s, at room temperature. All samples were prepared by dissolution of the studied compounds in a mixture of dried DMSO/CH_2Cl_2 in a 1:1 ratio, in a capillary that was placed in a quartz tube and frozen. For the spin-trapping assays, the tap was added to the compounds. The spin Hamiltonian parameters were determined by simulation of the experimental spectra using the computer program Bruker WinEPR/SimFonia.

4.2. Syntheses

4.2.1. Synthesis of H_2P1, CuP1 and H_2P2: general procedure

A solution of the appropriate free-base formyl-porphyrin derivative (**TPP-CHO** or **TPP-C_6H_4CHO**) or the copper(II) complex of **TPP-CHO** (25 mg), the 3-(diethylamino)phenol (5 equiv.) and *p*-toluenesulfonic acid (10 mol%) in a toluene/propanoic acid (2:1) mixture (1.5 mL) was stirred for 4 h at 120 °C. The mixture was then cooled to room temperature and added to a 3 M NaOAc aqueous solution (20 mL) and washed with water. The organic layer was extracted with CH_2Cl_2 and the solvent evaporated under reduced pressure. The crude was purified by column chromatography using CH_2Cl_2 and CH_2Cl_2/MeOH (98:2) as the eluents. The corresponding **H_2P1, CuP1** and **H_2P2** derivatives were isolated in very good yields, ranging from 81% to 91%.

H_2P1: Yield: 91%. ^{1}H NMR (300 MHz, $CDCl_3$): δ 8.90–8.76 (4H, m, H-β), 8.69 (1H, s, H-3), 8.55–8.45 (2H, m, H-β), 8.27–8.15 (4H, m, H-*o*-Ph), 8.14–8.06 (2H, m, H-*o*-Ph), 7.82–7.66 (9H, m, H-Ph), 7.65–7.55 (3H, m, H-Ph), 7.49 (2H, t, J = 7.0 Hz, H-Ph), 6.32 (2H, d, J = 8.4 Hz, H-6″), 6.20 (2H, s, H-3″), 5.88 (2H, d, J = 8.4 Hz, H-5″), 5.53 (1H, s, H-1′), 4.77 (2H, bs, -*O*H), 3.24 (8H, bq, J = 5.8, -*N*C$\underline{H}_2$CH$_3$), 1.08 (12H, bt, J = 5.8 Hz, -*N*CH$_2$C$\underline{H}_3$), −2.68 (2H, s, *N*H) ppm. ^{13}C NMR (75 MHz, $CDCl_3$): δ 155.2, 148.6, 142.3, 142.2, 142.0, 141.3, 135.0, 134.7, 134.5, 133.0, 130.3, 128.2, 127.9, 127.7, 127.4, 126.8, 126.6, 126.44, 126.37, 120.3, 120.1, 119.8, 119.6, 116.3, 105.0, 100.4, 44.4 (*N*C$\underline{H}_2$CH$_3$), 12.5 (*N*CH$_2$C$\underline{H}_3$) ppm. MS (ESI(+)): m/z 955.6 $[M+H]^+$. HRMS-ESI(+): m/z calculated for $C_{65}H_{59}O_2N_6$ $[M+H]^+$ 955.4694; found 955.4671.

CuP1: Yield: 85%. MS (ESI(+)): m/z 1016.5 $[M+H]^+$.

H_2P2: Yield: 88%. ^{1}H NMR (300 MHz, $CDCl_3$): δ 8.89–8.77 (4H, m, H-β), 8.76–8.71 (2H, m, H-β), 8.68 (1H, d, J = 4.9 Hz, H-β), 8.36–8.14 (4H, m, H-*o*-Ph), 8.00–7.88 (2H, m, H-*o*-Ph), 7.84–7.64 (9H, m, H-Ph), 7.47–7.27 (5H, m, H-Ph and H-3‴), 7.13–6.87 (2H, m, H-6‴), 6.78 (2H, d, J = 8.5 Hz, H-5‴), 6.49–6.13 (4H, m, H-2′,6′ and H-3′,5′), 5.45 (1H, s, H-1″), 3.55–3.25 (8H, m, -*N*C$\underline{H}_2$CH$_3$), 1.28–1.06 (12H, m, -*N*CH$_2$C$\underline{H}_3$), −2.63 (2H, s, *N*H) ppm. ^{13}C NMR (75 MHz, $CDCl_3$): δ 157.9, 157.6, 155.4, 142.4, 142.1, 141.7, 141.3, 141.1, 137.6, 136.5134.7, 133.6, 132.3, 130.6, 130.2, 129.3, 128.7, 128.1, 127.9, 127.6, 127.3, 126.9, 126.8, 126.3, 120.8, 120.6, 120.3, 120.1, 113.7, 113.3, 96.7, 46.2 (*N*C$\underline{H}_2$CH$_3$), 12.7 (*N*CH$_2$C$\underline{H}_3$) ppm. MS (ESI(+)): m/z 1031.7 $[M+H]^+$. HRMS-ESI(+): m/z calculated for $C_{71}H_{63}O_2N_6$ $[M+H]^+$ 1031.5007; found 1031.4989.

4.2.2. Synthesis of H_2P3

A round-bottomed flask containing a magnetic stirring bar was charged with **H_2P2** (20 mg) and *p*-chloranil (2.2 equiv.) and toluene (1 mL). The solution was stirred at reflux for 1 h. The cooled reaction mixture was washed with water and the aqueous layer was extracted with CH_2Cl_2. The organic layer was collected and concentrated under vacuum. The crude was purified by column chromatography using CH_2Cl_2 and CH_2Cl_2/MeOH (95:5) as the eluents.

H_2P3: Yield: 92%. ^{1}H NMR (300 MHz, $CDCl_3$): δ 8.97–8.75 (6H, m, H-β), 8.70 (1H, d, J = 4.9 Hz, H-β), 8.35–8.12 (6H, m, H-*o*-Ph), 8.06–7.93 (2H, m, H-*o*-Ph), 7.85–7.67 (9H, m, H-*m,p*-Ph), 7.53 (2H, d, J = 6.9 Hz, H-Ph), 7.46–7.29 (5H, m, H-Ph, H-3″ and H-6″), 7.19–7.04 (2H, m, H-4″), 6.96–6.70 (4H, m, H-2′,6′ and H-3′,5′), 3.82–3.26 (8H, m, -*N*C$\underline{H}_2$CH$_3$), 1.42–1.16 (12H, m, -*N*CH$_2$C$\underline{H}_3$), −2.61 (2H, s, *N*H) ppm. ^{13}C NMR (75 MHz, $CDCl_3$): δ 155.1, 148.6, 142.7, 142.0, 140.7, 136.1, 134.6, 134.5, 130.7, 128.3, 127.7, 126.8126.7, 126.2, 120.1, 104.8, 100.0, 44.4 (*N*C$\underline{H}_2$CH$_3$), 12.8 (*N*CH$_2$C$\underline{H}_3$) ppm. MS (ESI(+)): m/z 1011.7 $[M]^+$. HRMS-ESI(+): m/z calculated for $C_{71}H_{59}ON_6$ $[M]^+$ 1011.4745; found 1011.4727.

4.2.3. Synthesis of complexes CuP2 and CuP3

To a solution of the adequate free-base porphyrin **H_2P2** or **H_2P3** (20 mg) in a chloroform/methanol 2:1 mixture (4.5 mL) was added Cu(OAc)$_2$ and the mixture was heated at 60 °C for 20 min under stirring. Then, the reaction mixture was washed with water and the aqueous layer was extracted with CH_2Cl_2. The organic layer was collected and concentrated under vacuum. Compounds **CuP2** and **CuP3** were obtained in almost quantitative yields after crystallization from a CH_2Cl_2/hexane mixture.

CuP2: Yield: 98%. MS (ESI(+)): m/z calculated for $C_{71}H_{61}N_6O_2Cu$ $[M+H]^+$ 1092.4; found 1092.5.

CuP3: Yield: 97%. MS (ESI(+)): m/z calculated for $C_{71}H_{57}N_6OCu$ $[M]^+$ 1073.4; found 1073.6.

Funding

This work received financial support from PT national funds (FCT/MCTES, Fundação para a Ciência e Tecnologia and Ministério da Ciência, Tecnologia e Ensino Superior) through the projects UIDB/50006/2020 | UIDP/50006/2020,PTDC/QUI-QIN/28142/2017, PTDC/QUI-QOR/29426/2017, EXPL/QUI-OUT/1554/2021, UIDB/00100/2020 and UIDP/00100/2020.

Author Contributions

N.M.M.M and A.F.R.C carried out the synthesis and structural characterization of all compounds. C.Q performed the UV-Vis and fluorescence studies. A.L. performed the EPR studies. M.G.P.M.S.N and A.C.T. performed the analysis of the spectroscopic studies and A.M.G.S. designed, supervised the work and manuscript writing. All authors discussed, wrote and commented on the manuscript.

Declaration of competing interest

The authors declare that they have no known competing financial interests or personal relationships that could have appeared to influence

the work reported in this paper.

Data availability

Data will be made available on request.

Acknowledgements

A. M. G. Silva, A. Leite and V. V. Serra thank FCT for funding through program DL 57/2016 - Norma transitória. The authors also thank the University of Aveiro and the Portuguese NMR Network. Ana F. R. Cerqueira thanks FCT for her doctoral grant (SFRH/BD/135597/2018) and N.M.M. Moura thanks FCT for funding through program DL 57/2016 - Norma transitória (REF. 048-88-ARH/2018). We acknowledge the Research Center in Chemistry of University of Porto (CIQUP) for loaning the absolute luminescence quantum yield spectrometer (Quantaurus-QY C11347-11 spectrometer).

Appendix A. Supplementary data

Supplementary data to this article can be found online at https://doi.org/10.1016/j.dyepig.2023.111431.

References

[1] Wen Y, Jing N, Huo F, Yin C. Recent progress of organic small molecule-based fluorescent probes for intracellular pH sensing. Analyst 2021;146:7430–43. https://doi.org/10.1039/d1an01621k.
[2] Li K, Ren TB, Huan S, Yuan L, Zhang XB. Progress and perspective of solid-state organic fluorophores for biomedical applications. J Am Chem Soc 2021;143:21143–60. https://doi.org/10.1021/jacs.1c10925.
[3] Wagh SB, Maslivetc VA, La Clair JJ, Kornienko A. Lessons in organic fluorescent probe discovery. Chembiochem 2021;22:3109–39. https://doi.org/10.1002/cbic.202100171.
[4] Li Y, Chen Q, Pan X, Lu W, Zhang J. Development and challenge of fluorescent probes for bioimaging applications: from visualization to diagnosis. Top Curr Chem 2022;380:22. https://doi.org/10.1007/s41061-022-00376-8.
[5] Jin H, Yang M, Sun Z, Gui R. Ratiometric two-photon fluorescence probes for sensing, imaging and biomedicine applications at living cell and small animal levels. Coord Chem Rev 2021;446:214114. https://doi.org/10.1016/j.ccr.2021.214114.
[6] Lei Z, Zhang F. Molecular engineering of NIR-II fluorophores for improved biomedical detection. Angew Chem Int Ed 2021;60:16294–308. https://doi.org/10.1002/anie.202007040.
[7] Won M, Li M, Kim HS, Liu P, Koo S, Son S, et al. Visible to mid IR: a library of multispectral diagnostic imaging. Coord Chem Rev 2021;426:213608. https://doi.org/10.1016/j.ccr.2020.213608.
[8] Liu H, Wang S, Gao H, Shen Z. Reversible reaction-based fluorescent probes for dynamic sensing and bioimaging. Eur J Org Chem 2020;2020:5647–63. https://doi.org/10.1002/ejoc.202000359.
[9] Cardoso ICS, Amorim AL, Queirós C, Lopes SC, Gameiro P, de Castro B, et al. Microwave-assisted synthesis and spectroscopic properties of 4′-substituted rosamine fluorophores and naphthyl analogues. Eur J Org Chem 2012;2012:5810–7. https://doi.org/10.1002/ejoc.201200783.
[10] Plaza P, Dai Hung N, Martin MM, Meyer YH, Vogel M, Rettig W. Ultrafast internal charge transfer in a donor-modified rhodamine. Chem Phys 1992;168:365–73. https://doi.org/10.1016/0301-0104(92)87170-E.
[11] Zhang X-F, Su N, Lu X, Jia W. Benzoate-modified rhodamine dyes: large change in fluorescence properties due to photoinduced electron transfer. J Lumin 2016;179:511–7. https://doi.org/10.1016/j.jlumin.2016.07.031.
[12] Sabatini RP, Mark MF, Mark DJ, Kryman MW, Hill JE, Brennessel WW, et al. A comparative study of the photophysics of phenyl, thienyl, and chalcogen substituted rhodamine dyes. Photochem Photobiol Sci 2016;15:1417–32. https://doi.org/10.1039/C6PP00233A.
[13] Ding Y, Zhu W-H, Xie Y. Development of ion chemosensors based on porphyrin analogues. Chem Rev 2017;117:2203–56. https://doi.org/10.1021/acs.chemrev.6b00021.
[14] Liu Z, Li H, Tian Z, Liu X, Guo Y, He J, et al. Porphyrin-based nanoparticles: a promising phototherapy platform. Chempluschem 2022;87. https://doi.org/10.1002/cplu.202200156.
[15] Zhao X, Liu J, Fan J, Chao H, Peng X. Recent progress in photosensitizers for overcoming the challenges of photodynamic therapy: from molecular design to application. Chem Soc Rev 2021;50:4185–219. https://doi.org/10.1039/D0CS00173B.
[16] Lee H, Hong K-I, Jang W-D. Design and applications of molecular probes containing porphyrin derivatives. Coord Chem Rev 2018;354:46–73. https://doi.org/10.1016/j.ccr.2017.06.008.
[17] Sun X, Li D, Chen G, Zhang J. A series of new porphyrin dyads: the synthesis and photophysical properties. Dyes Pigments 2006;71:118–22. https://doi.org/10.1016/j.dyepig.2005.06.008.
[18] Mani T, Niedzwiedzki DM, Vinogradov SA. Generation of phosphorescent triplet states via photoinduced electron transfer: energy and electron transfer dynamics in Pt porphyrin–rhodamine B dyads. J Phys Chem A 2012;116:3598–610. https://doi.org/10.1021/jp301345h.
[19] Ferreira JAB, Serra VV, Sánchez-Coronilla A, Pires SMG, Faustino MAF, Silva AMS, et al. The Near-Mid-IR HOMO–LUMO gap in amide linked porphyrin–rhodamine dyads. Chem Commun 2013;49:8809–11. https://doi.org/10.1039/C3CC44925D.
[20] Pires SMG, Núñez C, Serra VV, Sánchez-Coronilla A, Faustino MAF, Simões MMQ, et al. Porphyrin-rhodamine conjugates as new materials with sensing ability. Dyes Pigments 2016;135:113–26. https://doi.org/10.1016/j.dyepig.2016.04.003.
[21] Lovell JF, Chan MW, Qi Q, Chen J, Zheng G. Porphyrin FRET acceptors for apoptosis induction and monitoring. J Am Chem Soc 2011;133:18580. https://doi.org/10.1021/ja2083569. –2.
[22] Ngen EJ, Rajaputra P, You Y. Evaluation of delocalized lipophilic cationic dyes as delivery vehicles for photosensitizers to mitochondria. Bioorg Med Chem 2009;17:6631–40. https://doi.org/10.1016/j.bmc.2009.07.074.
[23] Rajaputra P, Nkepang G, Watley R, You Y. Synthesis and in vitro biological evaluation of lipophilic cation conjugated photosensitizers for targeting mitochondria. Bioorg Med Chem 2013;21:379–87. https://doi.org/10.1016/j.bmc.2012.11.032.
[24] Ngen EJ, Xiao L, Rajaputra P, Yan X, You Y. Enhanced singlet oxygen generation from a porphyrin–rhodamine B dyad by two-photon excitation through resonance energy transfer. Photochem Photobiol 2013;89:841–8. https://doi.org/10.1111/php.12071.
[25] Zhu S, Yao S, Wu F, Jiang L, Wong K-L, Zhou J, et al. Platinated porphyrin as a new organelle and nucleus dual-targeted photosensitizer for photodynamic therapy. Org Biomol Chem 2017;15:5764–71. https://doi.org/10.1039/C7OB01003F.
[26] Moura NMM, Faustino MAF, Neves MGPMS, Duarte AC, Cavaleiro JAS. Vilsmeier-Haack formylation of Cu(II) and Ni(II) porphyrin complexes under microwaves irradiation. J Porphyr Phthalocyanines 2011;15:652–8. https://doi.org/10.1142/S1088424611003586.
[27] Zhou X, Chan KS. Synthesis of β-linked diporphyrins and their homo- and hetero-bimetallic complexes. J Org Chem 1998;63:99–104. https://doi.org/10.1021/jo971267s.
[28] Buchler JW. In: Smith KM, editor. In porphyrins and metalloporphyrins. Amsterdam: Elsevier; 1975. p. 157–231.
[29] Taniguchi M, Lindsey JS, Bocian DF, Holten D. Comprehensive review of photophysical parameters (ε, Φf, τs) of tetraphenylporphyrin (H2TPP) and zinc tetraphenylporphyrin (ZnTPP) – critical benchmark molecules in photochemistry and photosynthesis. J Photochem Photobiol C Photochem Rev 2021;46. https://doi.org/10.1016/j.jphotochemrev.2020.100401.
[30] Lan M, Zhao H, Yuan H, Jiang C, Zuo S, Jiang Y. Absorption and EPR spectra of some porphyrins and metalloporphyrins. Dyes Pigments 2007;74:357–62. https://doi.org/10.1016/j.dyepig.2006.02.018.
[31] Moura NMM, Núñez C, Faustino MAF, Cavaleiro JAS, Neves MGPMS, Capelo JL, et al. Preparation and ion recognition features of porphyrin-chalcone type compounds as efficient red-fluorescent materials. J Mater Chem C 2014;2:4772–83. https://doi.org/10.1039/c3tc32496f.
[32] De Luca G, Romeo A, Scolaro LM, Ricciardi G, Rosa A. Sitting-atop metallo-porphyrin complexes: experimental and theoretical investigations on such elusive species. Inorg Chem 2009;48:8493–507. https://doi.org/10.1021/ic9012153.
[33] Moura NMM, Valentini S, Cheptene V, Pucci A, Neves MGPMS, Capelo JL, et al. Multifunctional Porphyrin-based dyes for cations detection in solution and thermoresponsive low-cost materials. Dyes Pigments 2021;185:108897. https://doi.org/10.1016/j.dyepig.2020.108897.
[34] Radi S, Abiad C El, Moura NMM, Faustino MAF, Neves MGPMS. New hybrid adsorbent based on porphyrin functionalized silica for heavy metals removal: synthesis, characterization, isotherms, kinetics and thermodynamics studies. J Hazard Mater 2019;370:80–90. https://doi.org/10.1016/j.jhazmat.2017.10.058.
[35] Fleischer EB, Dixon F. Definitive evidence for the existence of the “sitting-atop” porphyrin complexes in nonaqueous solutions. Bioinorg Chem 1977;7:129–39. https://doi.org/10.1016/S0006-3061(00)80063-0.
[36] Fleischer EB, Wang JH. The detection of a type of reaction intermediate in the combination of metal ions with porphyrins. J Am Chem Soc 1960;82:3498–502. https://doi.org/10.1021/ja01499a004.
[37] Costa JIT, Oliveira E, Santos HM, Tomé AC, Neves MGPMS, Lodeiro C. Study of multiporphyrin compounds as colorimetric sitting-atop metal complexes: synthesis and photophysical studies. Chempluschem 2016;81:143–53. https://doi.org/10.1002/cplu.201500386.
[38] Wang C, Chi W, Qiao Q, Tan D, Xu Z, Liu X. Twisted intramolecular charge transfer (TICT) and twists beyond TICT: from mechanisms to rational designs of bright and sensitive fluorophores. Chem Soc Rev 2021;50:12656–78. https://doi.org/10.1039/D1CS00239B.
[39] Renault K, Chevalier A, Bignon J, Jacquemin D, Richard J-A, Romieu A. Coumarin-pyronin hybrid dyes: synthesis, fluorescence properties and theoretical calculations. ChemPhotoChem 2021;5:822–38. https://doi.org/10.1002/cptc.202100069.
[40] Almeida J, Silva AMN, Rebelo SLH, Cunha-Silva L, Rangel M, de Castro B, et al. Synthesis and coordination studies of 5-(4′-carboxyphenyl)-10,15,20-tris (pentafluorophenyl)porphyrin and its pyrrolidine-fused chlorin derivative. New J Chem 2018;42:8169–79. https://doi.org/10.1039/C7NJ05165D.
[41] Silva AMG, Leite A, Gonzalez P, Domingues MRM, Gameiro P, de Castro B, et al. Use of a porphyrin platform and 3,4-HPO chelating units to synthesize ligands with

N4 and O4 coordination sites. Tetrahedron 2011;67:7821–8. https://doi.org/10.1016/j.tet.2011.07.063.
[42] Cannistraro S, Vorst A, Jori G. EPR studies on singlet oxygen production by porphyrins. Photochem Photobiol 1978;28:257–9. https://doi.org/10.1111/j.1751-1097.1978.tb07704.x.
[43] Jeong H-G, Choi M-S. Design and properties of porphyrin-based singlet oxygen generator. Isr J Chem 2016;56:110–8. https://doi.org/10.1002/ijch.201500026.
[44] Teeuwen PCP, Melissari Z, Senge MO, Williams RM. Metal coordination effects on the photophysics of dipyrrinato photosensitizers. Molecules 2022;27:6967. https://doi.org/10.3390/molecules27206967.